JACS
JOURNAL OF THE AMERICAN CHEMICAL SOCIETY
Article
pubs.acs.org/JACS

Enhanced Electron Transport in Nb-Doped TiO_2 Nanoparticles via Pressure-Induced Phase Transitions

Xujie Lü,*[,†,‡] Wenge Yang,[‡,§,*] Zewei Quan,[∥] Tianquan Lin,[⊥] Ligang Bai,[†] Lin Wang,[‡,§] Fuqiang Huang,[⊥] and Yusheng Zhao*[,†]

[†]High Pressure Science and Engineering Center, University of Nevada, Las Vegas, Nevada 89154, United States

[‡]High Pressure Synergetic Consortium, Geophysical Laboratory, Carnegie Institution of Washington, Argonne, Illinois 60439, United States

[§]Center for High Pressure Science and Technology Advanced Research, Pudong, Shanghai 201203, People's Republic of China

[∥]Earth and Environmental Sciences Division, Los Alamos National Laboratory, Los Alamos, New Mexico 87545, United States

[⊥]CAS Key Laboratory of Materials for Energy Conversion, Shanghai Institute of Ceramics, Chinese Academy of Sciences, Shanghai 200050, People's Republic of China

Supporting Information

ABSTRACT: Anatase TiO_2 is one of the most important energy materials but suffers from poor electrical conductivity. Nb doping has been considered as an effective way to improve its performance in the applications of photocatalysis, solar cells, Li batteries, and transparent conducting oxide films. Here, we report the further enhancement of electron transport in Nb-doped TiO_2 nanoparticles via pressure-induced phase transitions. The phase transition behavior and influence of Nb doping in anatase Nb-TiO_2 have been systematically investigated by in situ synchrotron X-ray diffraction and Raman spectroscopy. The bulk moduli are determined to be 179.5, 163.3, 148.3, and 139.0 GPa for 0, 2.5, 5.0, and 10.0 mol % Nb-doped TiO_2, respectively. The Nb-concentration-dependent stiffness variation has been demonstrated: samples with higher Nb concentrations have lower stiffness. In situ resistance measurements reveal an increase of 40% in conductivity of quenched Nb-TiO_2 in comparison to the pristine anatase phase. The pressure-induced conductivity evolution is discussed in detail in terms of the packing factor model, which provides direct evidence for the rationality of the correlation of packing factors with electron transport in semiconductors. Pressure-treated Nb-doped TiO_2 with unique properties surpassing those in the anatase phase holds great promise for energy-related applications.

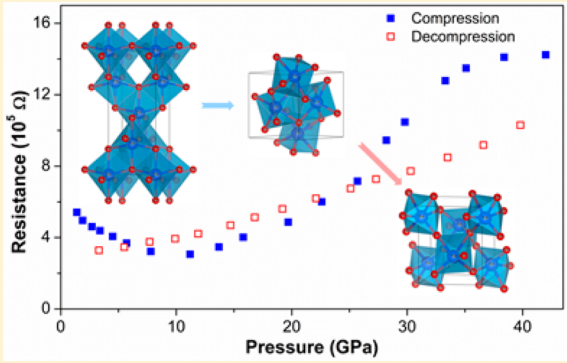

INTRODUCTION

Titanium dioxide (TiO_2) is one of the most attractive transition-metal oxides because of its superior physical and chemical properties, which have been widely applied in photocatalysis,[1,2] dye-sensitized solar cells (DSCs),[3,4] quantum dot solar cells,[5,6] lithium batteries,[7,8] sensors,[9] transparent conducting oxide (TCO) films,[10] etc. In energy conversion and storage applications, TiO_2 should possess outstanding charge separation and electron transport abilities, but the electron mobility of TiO_2 itself is low (0.1−4 $cm^2\ V\ s^{-1}$). Many efforts have been made to improve these properties, such as ion doping and semiconductor compositing.[11,12] Niobium (Nb) doping was demonstrated to be an effective way to enhance the performance of TiO_2 in the applications of photocatalysis, DSCs, Li batteries, and TCO films.[13−16]

TiO_2 has the three main polymorphs anatase, rutile, and brookite in nature and some synthetic forms (baddeleyite, columbite, TiO_2-B, etc.). The physical properties of TiO_2 are highly dependent on the crystal structure: for instance, the electron transport of the anatase phase is better than that of rutile phase and the same is true for the photocatalytic activities.[17] Therefore, the structural stability of the designed TiO_2 is crucial to its practical applications. The temperature dependence of structure evolution and size effects on phase transitions of TiO_2 has been fully investigated,[18−20] and the effect of ion doping on temperature-induced phase transitions was also studied.[21,22] In addition to temperature, pressure is another state parameter which provides a clean way to adjust interatomic distance and hence affect the crystal structure and electronic properties.

Pressure-induced phase transition has drawn great attention due to its fundamental importance in physics, chemistry, materials, and earth sciences.[23−25] It is also considered as a potential way to synthesize new phases which cannot be obtained under ambient pressure.[26,27] Pressure-induced phase

Received: October 22, 2013
Published: December 9, 2013

   dx.doi.org/10.1021/ja410810w | J. Am. Chem. Soc. 2014, 136, 419−426

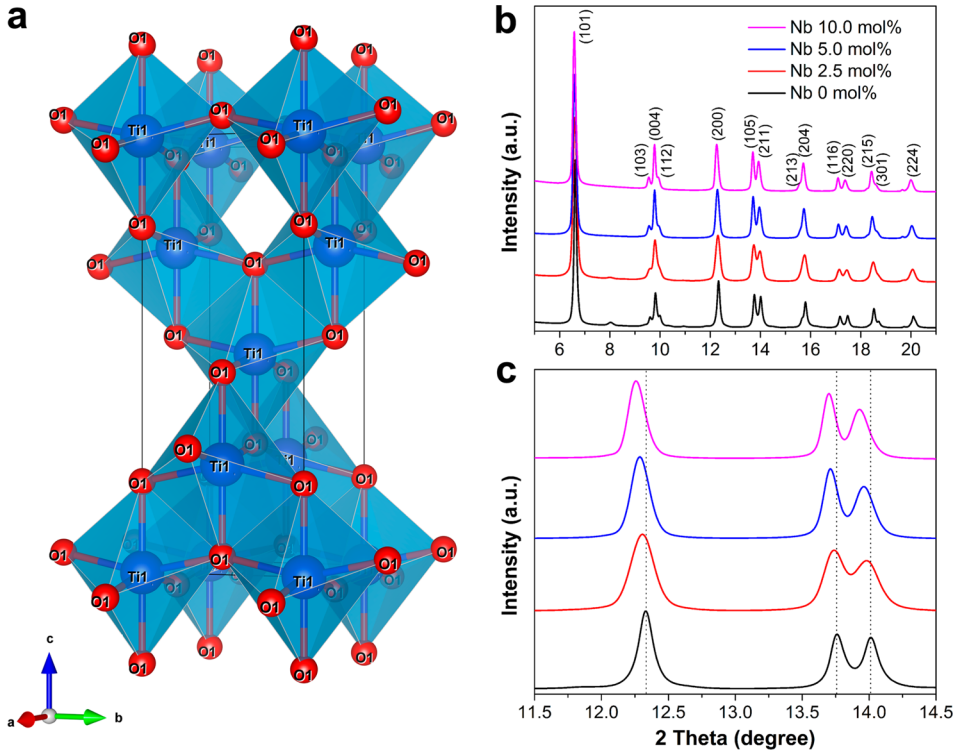

Figure 1. (a) Crystal structure of anatase TiO_2. (b) XRD patterns of as-prepared samples with different Nb concentrations from 0 to 10.0 mol %. (c) Magnified view of XRD patterns between 2θ values of 11.5 and 14.5°, from which one can see the obvious peak shift. For the undoped TiO_2 sample, there is a tiny peak at 2θ = 8° belonging to the brookite phase, which would disappear after Nb doping.

transitions in anatase TiO_2 (tetragonal, space group $I4_1/amd$) are particle size dependent:[28−30] crystallites with sizes >50 nm transform into columbite TiO_2 (orthorhombic α-PbO_2 type, $Pbcn$) at P > 5 GPa and then into the baddeleyite structure (monoclinic ZrO_2 type, $P2_1/c$) at P > 10 GPa (see crystal structures in Scheme S1 of the Supporting Information); 12−50 nm TiO_2 particles transform into the baddeleyite phase at 12−20 GPa; for smaller TiO_2 nanocrystals (<10 nm), pressure-induced amorphization was observed at P > 20 GPa. More recently, many studies indicated that the phase transitions of anatase TiO_2 depend on not only the size but also the morphology. For instance, the rice-shaped and the rod-shaped anatase samples exhibit very different compressibilities;[31] the TiO_2 nanowires show phase transition behavior different from that of the nanoparticles.[32] Thus far, there has still been no report on the structure stability and the effects of Nb doping on phase transitions in anatase Nb-TiO_2 under high pressure. In addition, it is highly demanding to develop new TiO_2-based materials with better performance than the anatase phase via state of the art methods.

One of the key purposes of high-pressure studies is the development of new high-pressure phases with novel or enhanced properties. Though intense research has been conducted on TiO_2 under high pressure and some new phases or structures have been obtained, there is still no report on enhanced performance of the designed TiO_2 in comparison with the corresponding anatase phase. In this study, we examine the pressure-dependent phase transitions in nanocrystalline doped TiO_2 with Nb concentrations from 0 to 10 mol % using in situ synchrotron X-ray diffraction (XRD) and Raman spectroscopy in diamond anvil cells (DACs) at room temperature and pressures up to 40 GPa. The phase transitions and the Nb-doping effects in various Nb-doped TiO_2 nanoparticles have been fully investigated and their bulk moduli determined. In situ high-pressure electrical resistance measurements manifested the enhanced electron-transport properties of pressure-treated Nb-doped TiO_2 nanoparticles. The transport evolution under high pressure was discussed in detail on the basis of crystal packing factor model. This work not only provides a systematic investigation into the stability and phase transitions of Nb-doped TiO_2 but also develops a new TiO_2-based material with better electron-transport performance in comparison to that of the pristine anatase phase.

RESULTS AND DISCUSSION

Anatase TiO_2 with a tetragonal crystal structure and space group $I4_1/amd$ is built up of edge- and corner-shared distorted TiO_6 octahedra (Figure 1a). The X-ray diffraction patterns of the as-prepared Nb-doped TiO_2 with different doping levels are shown in Figure 1b,c. All sharp XRD peaks of the samples can be assigned to the anatase phase (JCPDS No. 21-1272). The peaks shift to lower 2θ values with increasing Nb concentration because of the larger radius of Nb^{5+} (0.64 Å) in comparison to that of Ti^{4+} (0.61 Å), according to the Bragg equation $2d \sin\theta = \lambda$. The TEM images in Figure S1 of the Supporting Information show that the particle size of the TiO_2 nanoparticles is around 15 nm.

Nb-doped TiO_2 nanoparticles were loaded in symmetrical diamond anvil cells with neon as the pressure-transmitting medium for in situ high-pressure studies (see the Experimental Section for details). For better comparison, we loaded 0 and 5.0 mol % Nb-doped TiO_2 samples into one sample chamber and 2.5 and 10.0 mol % samples in another. Synchrotron XRD patterns of various Nb-doped TiO_2 samples collected at different pressures during compression and decompression

dx.doi.org/10.1021/ja410810w | J. Am. Chem. Soc. 2014, 136, 419−426

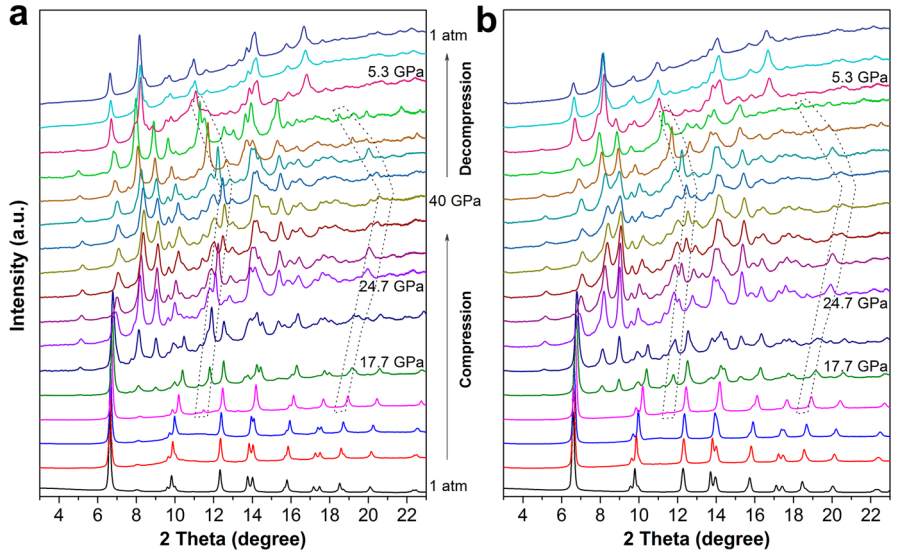

Figure 2. Synchrotron XRD patterns of Nb-doped TiO_2 nanoparticles with different Nb concentrations during compression and decompression: (a) 0 mol %; (b) 5.0 mol %. The marked peaks belong to solid Ne crystals under pressures higher than 8 GPa.

are shown in Figure 2 (0 and 5.0 mol % Nb-doped TiO_2) and Figure S2 (Supporting Information; 2.5 and 10.0 mol % samples). With an increase of pressure, all diffraction peaks shifted to larger 2θ values and the peak widths broadened gradually. For all of these Nb-doped TiO_2 samples, the transition from anatase to the denser baddeleyite phase was observed at ~17 GPa, in good agreement with previous reports for pure TiO_2.[28,33] The baddeleyite phase grew with a further increase of pressure, and the phase transition was complete at P > 25 GPa. The high-pressure phase was stable up to the highest pressure of 40 GPa in this study. During decompression, the baddeleyite phase transformed into a columbite structure at about 5 GPa and the columbite phase was recovered to ambient pressure. From the above results we found that the stability of the anatase phase and the pressure-induced phase transition behavior for the Nb-doped TiO_2 samples with different Nb concentrations are similar, which means the Nb-doped TiO_2 nanoparticles with various doping values up to 10.0 mol % are as stable as the undoped nanoparticles and are suitable for further optimization and operation in practical applications.

From the refinements of XRD data at pressures before the phase transition from anatase to baddeleyite, we plotted the unit cell volume versus pressure (P–V) curves, as shown in Figure 3a. Fitting P–V curves to a three-order Birch–Murnaghan equation of state (EOS) yields the equilibrium volume V_0 and bulk modulus B_0 with the derivative $B_0' = 4$. From Figure 3a, an increase of V_0 and a decrease of B_0 with an increase of Nb doping level were observed. The bulk moduli were determined to be 179.5, 163.3, 148.3, and 139.0 GPa for the 0, 2.5, 5.0, and 10.0 mol % Nb-doped TiO_2 nanoparticles, respectively, which suggests a decrease of elastic stiffness with an increase of Nb concentration. It has been reported that the B_0 values of anatase TiO_2 are 179 GPa from experiments and 189 GPa from calculations.[33] The evolution of lattice parameters (a/a_0 and c/c_0) of anatase TiO_2 under pressure are plotted in Figure 3b, indicating the anisotropic compressibility along different directions. The c axis was found to be more compressible than the a axis, and thus the volume shrinkages mainly contribute to the compression of the c axis. In Figure 2 we noticed that the (105) and (211) peaks at around 14° (2θ) approached each other during compression

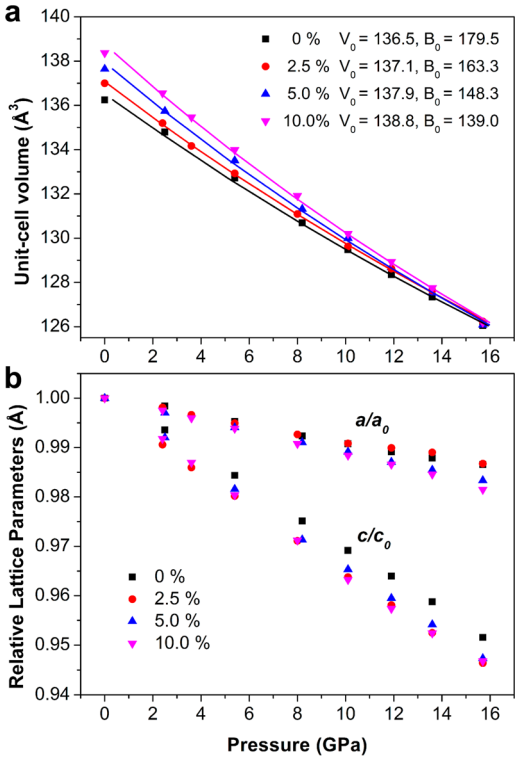

Figure 3. Evolutions of (a) the unit cell volumes and (b) lattice parameters of various Nb-doped TiO_2 samples under compression. The symbols are the data points, and the lines in panel a are fits of the data with the Birch–Murnaghan equation of state (EOS): $P(V) = 3B_0/2[(V_0/V)^{7/3} - (V_0/V)^{5/3}]\{1 + 3/4(B' - 4)[(V_0/V)^{2/3} - 1]\}$. A decrease of bulk modulus B_0 with an increase of Nb concentration was observed, and the compressibility of the c axis was found to be larger than that of the a axis.

and merged together eventually, owing to the relatively larger pressure-induced shortening in the longer apical Ti–O bonds along the c axis. Further compression induced destabilization of the TiO_6 octahedral arrangement and triggered the phase transition to a denser phase under higher pressures.

dx.doi.org/10.1021/ja410810w | J. Am. Chem. Soc. 2014, 136, 419–426

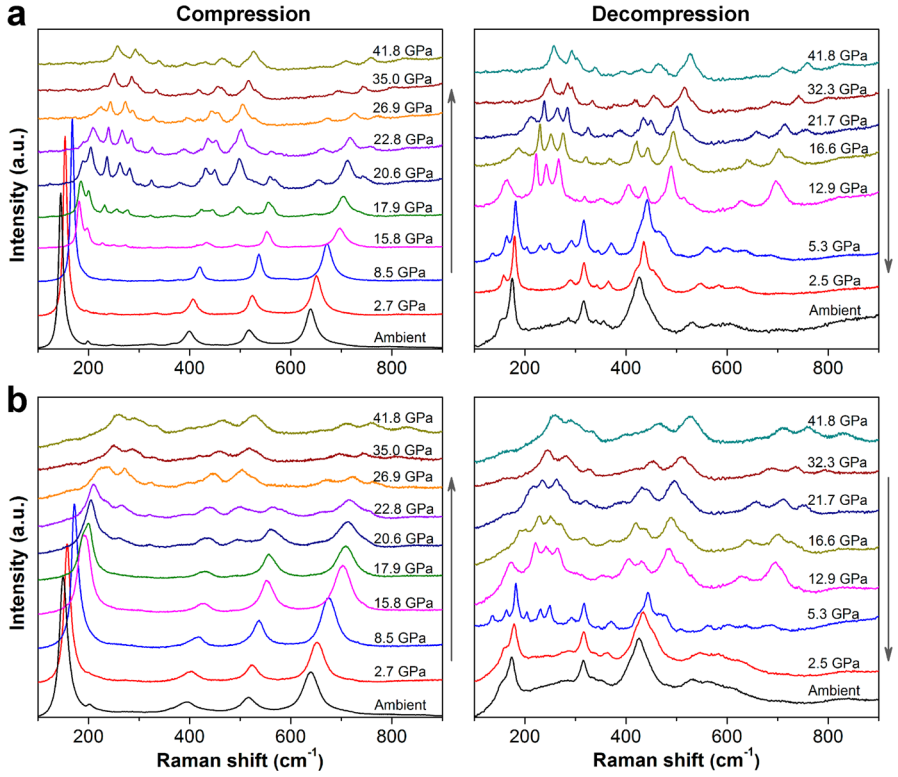

Figure 4. Raman spectra of Nb-doped TiO_2 nanoparticles collected during compression (left) and decompression (right) cycles at different Nb concentrations: (a) 0 mol %; (b) 5.0 mol %.

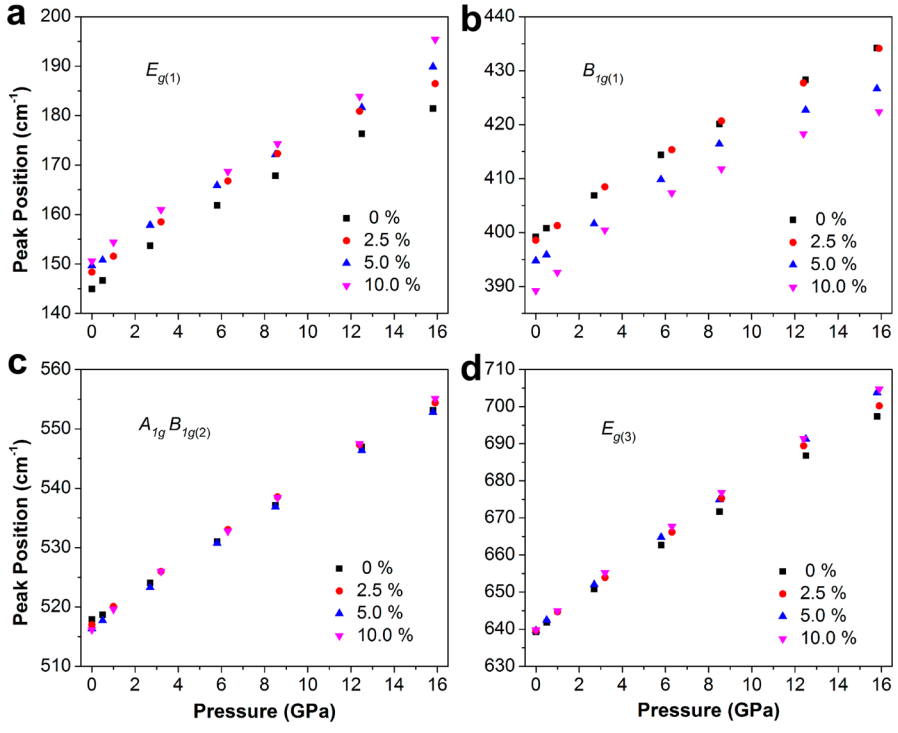

Figure 5. Pressure dependence of various Raman mode positions for Nb-doped anatase TiO_2 with different Nb concentrations: (a) $E_g(1)$ mode; (b) $B_{1g}(1)$ mode; (c) A_{1g} + $B_{1g}(2)$ modes; (d) $E_g(3)$ mode.

In order to further characterize the pressure-induced local structure evolution, we collected Raman spectra during compression−decompression cycles. Raman spectroscopy is highly sensitive to phase transitions occurring in TiO_2 and provides a detailed structural probe of local coordination environments.[29] Figure S3 (Supporting Information) shows the Raman spectra of various Nb-doped TiO_2 samples at ambient pressure, in which six Raman-active modes can be observed. Taking the undoped TiO_2 as an example, the six modes include three E_g modes centered around 144, 198, and 639 cm^{-1}

dx.doi.org/10.1021/ja410810w | J. Am. Chem. Soc. 2014, 136, 419−426

(designated as $E_g(1)$, $E_g(2)$ and $E_g(3)$, respectively), two B_{1g} modes at around 399 and 519 cm^{-1} (designated as $B_{1g}(1)$ and $B_{1g}(2)$), and one A_{1g} mode at 513 cm^{-1}. With an increase of Nb concentration, the broadening of all these Raman peaks was observed: the $E_g(1)$ mode has a blue shift, while the $B_{1g}(1)$ mode has a red shift; the $B_{1g}(2)$ + A_{1g} and $E_g(3)$ modes show very small red and blue shifts, respectively.

The Raman spectra measured during compression and decompression are shown in Figure 4 (0 and 5.0 mol % Nb-doped TiO_2) and Figure S4 (Supporting Information; 2.5 and 10.0 mol % samples). All of the Raman peaks show a blue shift during compression except for the $E_g(2)$ mode, which is too weak under pressure to determine its position. When the applied pressure exceeded 16 GPa, new peaks appeared, which indicate the onset of a phase transition from anatase to baddeleyite. With a further increase in pressure, the intensity of these baddeleyite peaks increased. The anatase and baddeleyite phases coexisted up to ~27 GPa, and then the pure baddeleyite structure was formed and remained at 41.8 GPa, the highest pressure measured here. Upon decompression, the baddeleyite phase transformed into the columbite phase at ~5 GPa, which remained at ambient pressure. All of the Nb-doped anatase TiO_2 samples show similar phase transitions under pressure, while the peaks broaden with an increase of Nb concentration. These results are in good agreement with the XRD data, which confirm that the phase transition behavior of Nb-doped TiO_2 is not sensitive to Nb concentration and that this species should be stable in particular applications.

The frequencies of Raman modes ($E_g(1)$, $B_{1g}(1)$, $B_{1g}(2)$ + A_{1g}, and $E_g(3)$) as a function of pressure are shown in Figure 5. The $E_g(1)$ mode arises from O−Ti−O bond-bending vibrations in which oxygen atoms in the TiO_6 octahedra undergo larger displacements than Ti atoms do under pressure:[34] that is, the oxygen atoms participate more actively in the octahedral compression. The blue shift of the $E_g(1)$ mode under pressure is caused by the shortening of the O−Ti−O bond. The obtained pressure coefficient of the $E_g(1)$ mode of undoped TiO_2 is 2.49 cm^{-1}/GPa, which is similar to the reported value for TiO_2 nanoparticles.[35] With an increase of Nb concentration, the pressure coefficient increases to 2.61, 2.70, and 2.81 cm^{-1}/GPa for 2.5, 5.0, and 10.0 mol % Nb-doped TiO_2, respectively, which indicates the faster reduction of bond lengths at higher Nb-doping levels. The pressure coefficients of other Raman modes have similar changing tendencies. All of these behaviors are in accordance with the bulk modulus decreasing with increasing Nb concentration. These results indicate that, although the phase transition behavior is not sensitive to Nb concentration, the stiffness of Nb-doped TiO_2 nanoparticles is dependent on the Nb-doping levels, which decreases with Nb concentration.

In order to explore the pressure-induced transport property evolution of Nb-doped TiO_2 nanoparticles, the sample with an Nb content of 5.0 mol % was selected to conduct the in situ resistance measurements under pressure. The resistance was determined by the Van de Pauw method using the equation $\exp(-\pi R_1/R_S) + \exp(-\pi R_2/R_S) = 1$, where R_1 and R_2 are the two resistances measured by the four-probe method (see details in the Supporting Information) and R_S is the sample resistance.[36] The resistance evolution of undoped TiO_2 was also measured for reference, which displays behavior similar to that for the Nb-doped sample (see Figures S5 and 6a, Supporting Information). As shown in Figure 6a, the resistance of Nb-doped TiO_2 decreases with increasing pressure in the

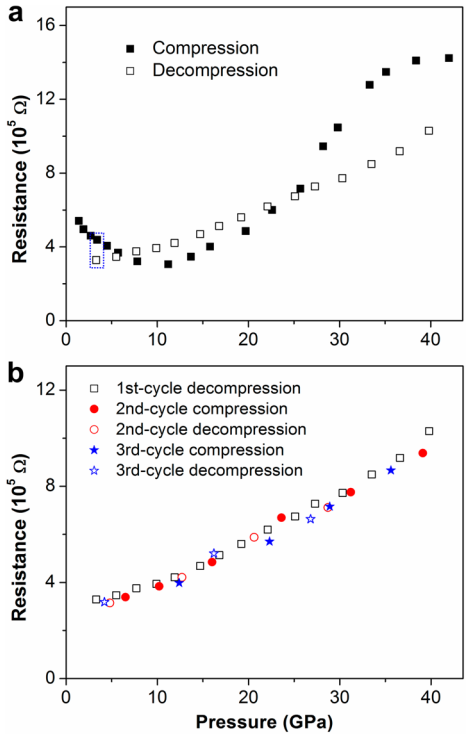

Figure 6. (a) Resistances of 5.0 mol % Nb-doped TiO_2 nanoparticles during the first compression−decompression cycle. (b) Resistance evolutions during the second and third compression−decompression cycles. Solid and open symbols represent compression and decompression procedures, respectively.

first stage (P < 3 GPa) because the contact between the nanoparticles becomes better during compression. As the pressure increases further, intimate contact between nanoparticles has been reached and the pressure-induced resistance drop between 3 and 12 GPa is associated with the broadening of the valence and conduction bands, caused by the shortening and bending of bonds.[37,38] Then the resistance begins to increase at 12−14 GPa, which corresponds to the phase transition from anatase to baddeleyite. The pressure for the phase transition deduced from resistance measurements (12−14 GPa) is somewhat lower than that determined from XRD and Raman results (~17 GPa). This deviation is probably due to the different hydrostatic conditions, because the resistance measurements were conducted without any pressure-transmitting medium. Nonhydrostatic pressure usually accelerates the pressure-induced phase transitions.[39] During further compression and subsequent decompression, the resistance increased and decreased with pressure, respectively. The resistance change is correlated to the crystal and electronic structures tuned by pressure.

A simple model based on the crystal packing factor (PF), which is computed by dividing the sum of spherical ion or atom volumes by the unit cell volume, was proposed to evaluate the electron transport ability and photocatalytic activity.[40] The concept came from Goodenough's idea that lower elastic stiffness can promote distortion, which increases the internal field, and it can be easily implemented using the packing factor.[41,42] It is a broadly applicable criterion for materials with similar compositions or structures. A detailed discussion about the PF model and its relationship to charge separation/transport and photocatalytic activity is given in the Supporting

dx.doi.org/10.1021/ja410810w | J. Am. Chem. Soc. 2014, 136, 419−426

Information. Briefly, a lower PF structure is more polarizable and deformable, which results in more efficient electron−hole separation and transport.[40] As demonstrated by the XRD and Raman analyses, the stiffness decreases with an increase of Nb-doping level, which provides additional evidence for the superior performance of Nb-doped TiO_2. The PF model can be employed to explain the different properties of various TiO_2 phases: e.g., anatase has a more loosely packed structure (density 3.89 g/cm^3, PF = 64.6%) and possesses higher conductivity and better photocatalytic activity. The baddeleyite TiO_2 has a denser structure (density 4.73 g/cm^3, PF = 78.1%), and thus poorer electron transport ability can be predicted. As mentioned above, the electron transport is also related to the valence and conduction band structures, which would broaden under compression and then cause the resistance drop between 3 and 12 GPa. Thus, there are two competing mechanisms influencing the electron transport: the broadening of valence and conduction bands ,which plays the dominant role before the phase transition from anatase to baddeleyite (<12 GPa), and the crystal packing factor, which is the main reason for a resistance increase after the phase transition and a resistance decrease during the subsequent decompression.

Pressure provides a clean way to adjust interatomic distances and thus the crystal packing factor, which can exclude other influencing factors, such as the composition, crystallinity, crystal size, and grain boundary. Therefore, high-pressure treatment would be a powerful tool to demonstrate and understand the structure−property relationship by tuning the interatomic distances. With an increase of pressure, the atomic distances decrease and the unit cell volume shrinks, increasing the PF value and hence the resistance. During decompression, the dense high-pressure structure transforms into a looser structure and the PF decreases, leading to the reduction of resistance. It is worth noting that the quenched columbite TiO_2 possesses significantly enhanced electrical conductivity (by ∼40%) in comparison with the pristine anatase TiO_2, although the anatase phase has a looser crystal structure. In order to exclude the contribution from the improved contact, we compared their resistances at the pressure of about 3 GPa (as marked by rectangle in Figure 6a), at which intimate contact between the nanoparticles has been achieved. Thus, the enhanced electrical conductivity should originate from the phase transition rather than the increased contact. The enhanced performance of quenched TiO_2 from high pressure may be caused by its special structure, which could be different from the phase prepared under ambient conditions.[43−45] This indicates that the high-pressure-treated Nb-doped TiO_2 would be a new promising material in energy-related applications such as photocatalysis and photovoltaics. In addition, the phase transition between baddeleyite and columbite is reversible during subsequent compression−decompression cycles, which was evidenced by the Raman spectra (Figure S6, Supporting Information). The resistance evolutions during the second and third compression−decompression cycles are shown in Figure 6b. The resistance increases monotonically during recompression and decreases during decompression, which confirms that the pressure-induced resistance change can be well explained by the packing factor model. The observation of resistance evolution under pressure is consistent with the prediction by the packing factor model. Therefore, our finding provides direct evidence to demonstrate the correlation between the packing factor and electron transport, and the rationality of using the packing factor model for ranking photocatalytic activities can be deduced, which is very helpful for understanding photocatalysis and developing new efficient photocatalysts.

■ CONCLUSIONS

In summary, the structure evolution and the influence of Nb doping on pressure-induced phase transitions of Nb-doped TiO_2 nanoparticles were systematically investigated by high-pressure synchrotron X-ray diffraction and Raman spectroscopy. The phase transitions from anatase to baddeleyite at ∼17 GPa during compression and the further transformation of the baddeleyite phase into the columbite phase at ∼5 GPa during decompression were observed for all of the TiO_2 samples with Nb concentrations from 0 to 10.0 mol %. The bulk moduli were calculated to be 179.5, 163.3, 148.3, and 139.0 GPa for 0, 2.5, 5.0, and 10.0 mol % Nb-doped TiO_2, respectively. The decrease of the bulk modulus as the Nb doping level increases and the increase of pressure coefficients of the Raman modes indicate the Nb-concentration-dependent stiffness variation: that is, a sample with a higher Nb concentration has lower stiffness. In situ high-pressure resistance measurements on the Nb-doped TiO_2 shows a significant enhancement in electron-transport properties of the pressure-treated TiO_2 in comparison to the pristine anatase phase. The pressure-induced evolution of transport performance can be well explained by the packing factor model. This study not only reveals the phase transition behaviors of various Nb-doped TiO_2 and develops a better TiO_2 material than the pristine anatase phase for energy-related applications but also provides direct evidence for the rationality of the packing factor model for ranking the electron transport.

■ EXPERIMENTAL SECTION

Sample Preparation and Microstructure Characterization. The synthesis of Nb-doped TiO_2 has been described in detail in previous work.[13] Briefly, stoichiometric niobium powder (e.g., 0.002 mol for a 10 mol % sample) and tetrabutyltitanate (0.018 mol) were added into a solution containing hydrogen peroxide and ammonia (30 mL, 5/1 v/v) with continuous stirring to obtain the precursor. The precursor was then transferred into a Teflon-lined autoclave (50 mL capacity, 70% filling). The autoclave was heated to 180 °C at a rate of 3 °C min^{-1} and maintained for 20 h. The resulting precipitates were washed with deionized water until pH 7 was reached and dried at 100 °C for 6 h. Other samples with different Nb contents (0, 2.5, and 5.0 mol %) were prepared by following the same procedure. The morphology and microstructure of as-prepared Nb-doped TiO_2 samples were investigated by a field-emission transmission electron microscope (JEOL JEM 2100F, working at 200 kV).

In Situ High-Pressure Characterizations. A symmetrical DAC was employed to generate high pressure. A rhenium gasket was preindented to 30 μm in thickness followed by laser-drilling the central part to form a 150 μm diameter hole to serve as the sample chamber. Precompressed TiO_2 powder pallets and two small ruby balls were loaded into the chamber. The 0 and 5.0 mol % samples were loaded in one sample chamber side by side to provide almost the same pressure environment for good comparison, and the same was done for the 2.5 and 10.0 mol % samples, as shown in Figure S7 of the Supporting Information. Neon was used as the pressure-transmitting medium, and the pressures were determined by the ruby fluorescence method.[46] The in situ high-pressure angle-dispersive X-ray diffraction (ADXD) experiments were carried out at the 16 ID-B station of the High-Pressure Collaborative Access Team (HPCAT) at the Advanced Phonon Source (APS), Argonne National Laboratory (ANL). A focused monochromatic X-ray beam about 5 μm in diameter (fwhm) with a wavelength of 0.4066 Å was used for the diffraction experiments. The diffraction data were recorded by a MAR345 image plate, and then the two-dimensional (2D) images were integrated to one-dimensional (1D) patterns with the Fit2D program.

dx.doi.org/10.1021/ja410810w | J. Am. Chem. Soc. 2014, 136, 419−426

High-pressure Raman spectra were measured by a Raman spectrometer with a 532.1 nm excitation laser at HPCAT.

In Situ High-Pressure Resistance Measurements. Electrical resistance measurements were conducted with a four-probe resistance test system in a diamond-anvil cell at pressures up to 42 GPa. A boron nitride (BN) layer was inserted between the Re gasket and diamond culet to provide the electrical insulation between the electrical leads and metal gasket. Four platinum leads (2 μm thick) were arranged to contact the sample in the chamber (see Figure S8, Supporting Information). A Keithley 6221 current source, 2182A nanovoltmeter, and 7001 switch system were used as the current supply, voltmeter, and voltage/current switcher, respectively. The resistance was determined by the Van de Pauw method (see details in the Supporting Information).[36]

■ ASSOCIATED CONTENT

Supporting Information

Text and figures giving details of four-probe resistance measurements in DAC, crystal structures of various TiO_2 phases, TEM images, synchrotron XRD and Raman spectra of 2.5 and 10.0 mol % Nb-doped TiO_2 samples, $R-P$ curve of undoped TiO_2, Raman spectra during various compression and decompression cycles, and microphotographs of the samples and ruby balls in DAC. This material is available free of charge via the Internet at http://pubs.acs.org.

■ AUTHOR INFORMATION

Corresponding Author

*xujie@aps.anl.gov; wyang@ciw.edu; yusheng.zhao@unlv.edu

Notes

The authors declare no competing financial interest.

■ ACKNOWLEDGMENTS

The UNLV High Pressure Science and Engineering Center (HiPSEC) is a DOE-NNSA Center of Excellence supported by Cooperative Agreement DE-NA0001982. HPSynC is supported by the EFree, an Energy Frontier Research Center funded by the DOE-BES under Grant DE-SC0001057. HPCAT operations are supported by the DOE-NNSA under Award DE-NA0001974 and DOE-BES under Award DE-FG02-99ER45775, with partial instrumentation funding by the NSF. The gas loading was performed at GeoSoilEnviroCARS, APS, ANL, supported by EAR-1128799 and DE-FG02-94ER14466. The samples synthesis was conducted at Shanghai Institute of Ceramics, Chinese Academy of Sciences, supported by NSF of China Grant No. 51125006 and 91122034. The authors thank H. K. Mao, Y. Ding, M. Baldini, J. Y. Wang, K. Li, R. Ferry, G. Y. Shen, Y. Meng, C. Park, J. Smith, S. Sinogeikin, E. Rod, Q. S. Zeng, B. Lavina, and S. Tkachev for their valuable suggestions and technical support.

■ REFERENCES

(1) Linsebigler, A. L.; Lu, G.; Yates, J. T., Jr. *Chem. Rev.* **1995**, *95*, 735.
(2) Xu, C.; Yang, W.; Guo, Q.; Dai, D.; Chen, M.; Yang, X. *J. Am. Chem. Soc.* **2013**, *135*, 10206.
(3) O'Regan, B.; Grätzel, M. *Nature* **1991**, *353*, 737.
(4) Son, H. J.; Prasittichai, C.; Mondloch, J. E.; Luo, L.; Wu, J.; Kim, D. W.; Farha, O. K.; Hupp, J. T. *J. Am. Chem. Soc.* **2013**, *135*, 11529.
(5) Robel, I.; Subramanian, V.; Kuno, M.; Kamat, P. V. *J. Am. Chem. Soc.* **2006**, *128*, 2385.
(6) Etgar, L.; Gao, P.; Xue, Z.; Peng, Q.; Chandiran, A. K.; Liu, B.; Nazeeruddin, M. K.; Grätzel, M. *J. Am. Chem. Soc.* **2012**, *134*, 17396.
(7) Chen, J. S.; Tan, Y. L.; Li, C. M.; Cheah, Y. L.; Luan, D.; Madhavi, S.; Boey, F. Y. C.; Archer, L. A.; Lou, X. W. *J. Am. Chem. Soc.* **2010**, *132*, 6124.
(8) Shen, L.; Zhang, X.; Li, H.; Yuan, C.; Cao, G. *J. Phys. Chem. Lett.* **2011**, *2*, 3096.
(9) Zheng, Q.; Zhou, B.; Bai, J.; Li, L.; Jin, Z.; Zhang, J.; Li, J.; Liu, Y.; Cai, W.; Zhu, X. *Adv. Mater.* **2008**, *20*, 1044.
(10) Noh, J. H.; Han, H. S.; Lee, S.; Kim, D. H.; Park, J. H.; Park, S.; Kim, J. Y.; Jung, H. S.; Hong, K. S. *J. Phys. Chem. C* **2010**, *114*, 13867.
(11) Liu, G.; Yang, H. G.; Wang, X.; Cheng, L.; Pan, J.; Lu, G. Q.; Cheng, H. M. *J. Am. Chem. Soc.* **2009**, *131*, 12868.
(12) Lü, X.; Huang, F.; Mou, X.; Wang, Y.; Xu, F. *Adv. Mater.* **2010**, *22*, 3719.
(13) Lü, X.; Mou, X.; Wu, J.; Zhang, D.; Zhang, L.; Huang, F.; Xu, F.; Huang, S. *Adv. Funct. Mater.* **2010**, *20*, 509.
(14) Furubayashi, Y.; Hitosugi, T.; Yamamoto, Y.; Inaba, K.; Kinoda, G.; Hirose, Y.; Shimada, T.; Hasegawa, T. *Appl. Phys. Lett.* **2005**, *86*, 252101.
(15) Das, C.; Roy, P.; Yang, M.; Jha, H.; Schmuki, P. *Nanoscale* **2011**, *3*, 3094.
(16) Fehse, M.; Cavaliere, S.; Lippens, P. E.; Savych, I.; Iadecola, A.; Monconduit, L.; Jones, D. J.; Rozière, J.; Fischer, F.; Tessier, C.; Stievano, L. *J. Phys. Chem. C* **2013**, *117*, 13827.
(17) Park, N. G.; van de Lagemaat, J.; Frank, A. J. *J. Phys. Chem. B* **2000**, *104*, 8989.
(18) Barnard, A. S.; Curtiss, L. A. *Nano Lett.* **2005**, *5*, 1261.
(19) Zhang, H.; Banfield, J. F. *J. Phys. Chem. B* **2000**, *104*, 3481.
(20) Djaoued, Y.; Badilescu, S.; Ashrit, P. V.; Bersani, D.; Lottici, P. P.; Robichaud, J. *J. Sol-Gel Sci. Technol.* **2002**, *24*, 255.
(21) Cao, Y.; He, T.; Zhao, L.; Wang, E.; Yang, W.; Cao, Y. *J. Phys. Chem. C* **2009**, *113*, 18121.
(22) Arbiol, J.; Cerda, J.; Dezanneau, G.; Cirera, A.; Peiro, F.; Cornet, A.; Morante, J. R. *J. Appl. Phys.* **2002**, *92*, 853.
(23) Zahn, D.; Leoni, S. *Phys. Rev. Lett.* **2004**, *92*, 250201.
(24) Deb, S. K.; Wilding, M.; Somayazulu, M.; McMillan, P. F. *Nature* **2001**, *414*, 528.
(25) Sharma, S. M.; Karmakar, S.; Sikka, S. K.; Teredesai, P. V.; Sood, A. K.; Govindaraj, A.; Rao, C. N. R. *Phys. Rev. B: Condens. Matter Mater. Phys.* **2001**, *63*, 205417.
(26) Wu, Z.; Cohen, R. E. *Phys. Rev. Lett.* **2005**, *95*, 037601.
(27) Kawai, N.; Atou, T.; Ito, S.; Yubuta, K.; Kikuchi, M.; Nakamura, K. G.; Kondo, K. *Adv. Mater.* **2007**, *19*, 2375.
(28) Swamy, V.; Kuznetsov, A.; Dubrovinsky, L. S.; McMillan, P. F.; Prakapenka, V. B.; Shen, G.; Muddle, B. C. *Phys. Rev. Lett.* **2006**, *96*, 135702.
(29) Swamy, V.; Kuznetsov, A.; Dubrovinsky, L. S.; Caruso, R. A.; Shchukin, D. G.; Muddle, B. C. *Phys. Rev. B: Condens. Matter Mater. Phys.* **2005**, *71*, 184302.
(30) Pischedda, V.; Hearne, G. R.; Dawe, A. M.; Lowther, J. E. *Phys. Rev. Lett.* **2006**, *96*, 035509.
(31) Park, S. W.; Jang, J. T.; Cheon, J.; Lee, H. H.; Lee, D. R.; Lee, Y. *J. Phys. Chem. C* **2008**, *112*, 9627.
(32) Li, Q.; Cheng, B.; Yang, X.; Liu, R.; Liu, B.; Liu, J.; Chen, Z.; Zou, B.; Cui, T.; Liu, B. *J. Phys. Chem. C* **2013**, *117*, 8516.
(33) Arlt, T.; Bermejo, M.; Blanco, M. A.; Gerward, L.; Jiang, J. Z.; Staun Olsen, J.; Recio, J. M. *Phys. Rev. B: Condens. Matter Mater. Phys.* **2000**, *61*, 14414.
(34) Ohsaka, T.; Izumi, F.; Fujiki, Y. *J. Raman Spectrosc.* **1978**, *7*, 321.
(35) Wang, Z.; Saxena, S. K.; Pischedda, V.; Liermann, H. P.; Zha, C. S. *J. Phys.-Condens. Mater.* **2001**, *13*, 8317.
(36) van der Pauw, L. J. *Philips Res. Rep.* **1958**, *13*, 1.
(37) Ma, Y.; Eremets, M.; Oganov, A. R.; Xie, Y.; Trojan, I.; Medvedev, S.; Lyakhov, A. O.; Valle, M.; Prakapenka, V. *Nature* **2009**, *458*, 182.
(38) Arai, K.; Kumata, K.; Kadota, K.; Yamamoto, K.; Namikawa, H.; Saito, S. *J. Non-Cryst. Solids* **1973**, *13*, 131.
(39) Goncharov, A. F. *High Pressure Res.* **1992**, *8*, 607.
(40) Lin, X.; Wu, J.; Lu, X.; Shan, Z.; Wang, W.; Huang, F. *Phys. Chem. Chem. Phys.* **2009**, *11*, 10047.

(41) Goodenough, J. B.; Zhou, J. S. *Chem. Mater.* **1998**, *10*, 2980.
(42) Goodenough, J. B.; Menyuk, N.; Dwight, K.; Kafalas, J. A. *Phys. Rev. B: Condens. Matter Mater. Phys.* **1970**, *2*, 4640.
(43) Sharma, S. M.; Sikka, S. K. *Prog. Mater. Sci.* **1996**, *40*, 1.
(44) Kawai, N.; Atou, T.; Ito, S.; Yubuta, K.; Kikuchi, M.; Nakamura, K. G.; Kondo, K. *Adv. Mater.* **2007**, *19*, 2375.
(45) Lü, X.; Hu, Q.; Yang, W.; Bai, L.; Sheng, H.; Wang, L.; Huang, F.; Wen, J.; Miller, D. J.; Zhao, Y. *J. Am. Chem. Soc.* **2013**, *135*, 13947.
(46) Mao, H. K.; Xu, J.; Bell, P. M. *J. Geophys. Res.* **1986**, *91*, 4673.